

1 Uppermost mantle velocity beneath the Mid-Atlantic Ridge and transform

2 faults in the equatorial Atlantic Ocean

6 Abstract

7 Seismic rays travelling just below the Moho provide insights into the thermal and compositional
8 properties of the upper-mantle, and can be detected as *Pn* phases from regional earthquakes. Such
9 phases are routinely identified in the continents, but in the oceans, detection of *Pn* phases is limited
10 by a lack of long-term instrument deployments. We present estimates of upper-mantle velocity in
11 the equatorial Atlantic Ocean from *Pn* arrivals beneath, and flanking, the Mid-Atlantic Ridge, and
12 across several transform faults. We analyzed waveforms from 50 earthquakes with magnitude
13 $M_w > 3.5$, recorded over 12 months in 2012–2013 by five autonomous hydrophones and a
14 broadband seismograph located on the St. Peter and St. Paul archipelago. The resulting catalog of
15 152 ray paths allows us to resolve spatial variations in upper-mantle velocities, which are
16 consistent with estimates from nearby wide-angle seismic experiments. We find relatively high
17 velocities near to the St. Paul transform system ($\sim 8.4 \text{ km s}^{-1}$), compared to lower ridge-parallel
18 velocities ($\sim 7.7 \text{ km s}^{-1}$). Hence, this method is able to resolve ridge-transform scale velocity
19 variations. Ray paths in lithosphere younger than 10 Myr have mean velocities of $7.9 \pm 0.5 \text{ km s}^{-1}$
20 1 , which is slightly lower than those sampling lithosphere older than 20 Myr ($8.1 \text{ km s}^{-1} \pm 0.3 \text{ s}^{-1}$).
21 There is no apparent systematic relationship between velocity and ray azimuth, which could be
22 due to thickened lithosphere or complex mantle upwelling, although uncertainties in our velocity
23 estimates may obscure such patterns. We also do not find any correlation between *Pn* velocity and

24 shear wave speeds from the global SL2013sv model at depths < 150 km. Our results demonstrate
25 that data from long-term deployments of autonomous hydrophones can be used to obtain rare and
26 insightful estimates of uppermost mantle velocities over hundreds of kilometers, in otherwise
27 inaccessible parts of the deep oceans.

28

29 **Introduction**

30 Seismic velocity measurements provide a useful tool for investigating spatial variations in upper-
31 mantle properties, such as temperature and anisotropy, with implications for melt supply and
32 mantle heterogeneity (e.g. Lin and Phipps Morgan, 1992; Dunn *et al.*, 2005). These measurements
33 are relatively straightforward to obtain on the continents (e.g. Chulick and Mooney, 2002; Chulick
34 *et al.*, 2013). However, it remains challenging and expensive to measure upper-mantle seismic
35 velocity in the deep ocean, due to its remote location and difficulties in deploying long-term
36 instruments on the seafloor. Pn phases are rays that are critically refracted at the Moho and
37 propagate along the top of the uppermost mantle (e.g. Linehan, 1940; Brandsdottir and Menke,
38 1997). At the Mid-Atlantic Ridge (MAR) from 10°N to 35°N , Pn arrivals from 48 individual ray
39 paths were recorded with hydrophones, and used to investigate upper-mantle velocities, giving a
40 mean velocity of $8.0 \pm 0.1 \text{ km s}^{-1}$ (Dziak *et al.*, 2004). This velocity estimate was higher than that
41 from nearby active source seismic experiments along the ridge axis ($7.5\text{--}7.9 \text{ km s}^{-1}$; Canales *et al.*,
42 2000), probably due to the effects of younger and thinner oceanic lithosphere being sampled by
43 the refraction profiles, and the effects of averaging velocities across all rays. Despite such
44 advances, upper-mantle velocities in the deep oceans remain poorly constrained, and the potential
45 for hydrophone-recorded Pn phases to resolve spatial variations in upper-mantle velocity has not
46 yet been sufficiently tested.

47 Here, we use Pn arrivals from regional earthquakes to constrain upper-mantle velocity in
48 the equatorial Atlantic Ocean. Arrivals were recorded by a combination of five moored
49 hydrophones and a single seismograph station installed on the St. Peter and St. Paul islets, giving
50 152 ray paths that sample mantle conditions both on- and off-axis, and across the St. Paul transform
51 system. Our study is coincident with several mantle velocity estimates from a wide-angle seismic
52 experiment (Le Pichon *et al.*, 1965), and hence has the opportunity to validate spatial variations in
53 velocity revealed by groups of similar ray paths.

54

55 ***Equatorial Atlantic Ocean***

56 In the equatorial Atlantic Ocean (10°N–5°S and 34°W–21°W), the MAR is offset by some
57 of the longest transform faults on Earth, including the Strakhov, St. Paul, and Romanche
58 transforms (Figure 1). The St. Paul transform system consists of four transform faults and three
59 intra-transform ridge segments that accommodate an offset of 630 km. The northwest transform
60 fault is currently undergoing transpression, giving rise to the ~200 km-long and ~30 km-wide
61 Atobá ridge (Maia *et al.*, 2016), and also uplift of 1.5mm yr⁻¹ at the St. Peter and St. Paul islets
62 (Campos *et al.*, 2010; Maia *et al.*, 2016). Other transforms in the system do not host topographic
63 highs or an island related to transpression, and hence presumably are not experiencing uplift. In
64 the three intervening spreading segments, seafloor spreading is slow, at ~16 mm yr⁻¹ average half
65 rate (DeMets *et al.*, 2010). Faulting plays an important role in crustal accretion, and seismicity
66 rates are relatively high, providing a useful tool to investigate the properties of the crust and upper
67 mantle, as well as deformation at long-offset strike-slip systems (e.g. Francis *et al.*, 1978;
68 Abercrombie and Ekstrom, 2001; de Melo and do Nascimento, 2018).

69 **Methods**

70 **Waveform Data**

71 We analyzed *Pn* arrivals in waveform data recorded by a combination of five moored
72 autonomous hydrophones and one land-based seismograph (Figure 2). The five autonomous
73 hydrophone instruments were deployed during two separate experiments: stations EA2 and EA8
74 were part of the Equatorial Atlantic (EA) array (Smith et al., 2012). Data were recorded at 16-bit
75 resolution and a sampling rate of 250 Hz; for further details on these hydrophone instruments see
76 Fox *et al.* (2001). Hydrophones H2, H4, H5 were deployed during the COLD Mantle Exhumation
77 and Intra-transform Accretion experiment (COLMEIA; Maia *et al.*, 2014, 2016), and recorded
78 data at 24 bit-resolution with a sampling rate of 240 Hz; for further instrument details see D'Eu
79 *et al.* (2012). We also used waveform data recorded by a three-component broadband
80 seismograph installed at the St. Peter and St. Paul Archipelago Scientific Station on the
81 Belmonte islet (ASPSP; de Melo and do Nascimento, 2018). This station is operated by the
82 Seismological Laboratory of Federal University of Rio Grande do Norte in cooperation with the
83 Brazilian Navy. The sparse distribution and mixed instrument types we used means that data
84 coverage is uneven, as shown in Figure 1b. Waveform data were examined for the time period
85 from July 2012 to July 2013, with recording intervals dictated by technical challenges and vessel
86 schedules (Figure 1b).

87

88 ***Pn* analysis**

89 Prior to manually picking *Pn* arrivals, we applied a 6–20 Hz Butterworth bandpass filter to
90 the hydrophone data in order to suppress unwanted noise. A bandpass filter with range 4–12 Hz
91 was applied prior to picking arrivals from the ASPSP seismograph, to suppress additional
92 microseism noise due to its island location. Based upon origin time, events were manually

93 associated with earthquakes in the International Seismological Center Bulletin (ISC), yielding
94 hypocenter locations, origin times, and magnitudes ranging from 3.5 to 5.4 M_w. Earthquakes
95 mostly occur due to strike-slip faulting along the Strakhov, St. Paul, and Romanche transform
96 faults, with additional events due to extension along the intervening spreading ridge segments
97 (Figure 2a). Example arrivals from three events are shown in Figures 3 and 4, highlighting the
98 typical response to strike-slip and normal faulting earthquakes ranging in magnitude from 4.6 to
99 5.3 M_w.

100 Typical *Pn*-arrivals are emergent, and have low signal-to-noise ratio (SNR; noted in
101 Figures 3 and 4), making pick identification challenging. Given the mixed nature of our network
102 and often noisy arrivals, picks were made based on the onset of emergent energy combined with
103 changes in SNR, waveform character and amplitude. The observation of linear move-out,
104 consistent with upper mantle velocity, added confidence to our picks, since this moveout is evident
105 across the hydrophone array stations due to wave propagation along the crust-mantle interface (see
106 common-receiver plots in Supplementary Figures S1–S6). *P*-arrivals are easily distinguished from
107 *T*-phase arrivals, which arrive much later than *P*-arrivals, are emergent in character, and are higher
108 in amplitude than *P*-arrivals (see hydrophone H5 in Figure 4). The catalog of detected events is
109 given in Table S1.

110 In order to further test whether the detected arrivals were *Pn* phases, we compared the
111 observed travel times to those predicted by the global iasp91 velocity model (Kennett and Engdahl,
112 1991). For each source-receiver ray path, we calculated the predicted *Pn* arrival time using iasp91,
113 with the addition of a station-dependent delay to account for the propagation time from seafloor to
114 hydrophone. This delay (1.2–2.5 s, see Table 1) was estimated using the hydrophone mooring cable
115 length at each station, and the local water sound velocity estimated from the Global Ocean Sound

116 Speed Profile Library (Barlow, 2019). The predicted Pn arrival times differ from the observed Pn
117 arrivals by 5–10 s (Figures 3 and 4), a difference which arises since the iasp91 model contains a
118 crustal layer that is much thicker (30 km) than that expected in the oceans (\sim 6 km). Hence, the
119 differences in observed and predicted Pn arrival time are probably dominated by this additional
120 crustal layer thickness in the velocity model, plus earthquake location and origin time uncertainties.
121 Although these differences are evident, the waveform character and linear move-out velocity give
122 us confidence in our identification of these emergent phases as Pn arrivals.

123 ISC origin times were subtracted from the Pn arrival times to obtain travel times for each
124 ray path (i.e. each event-station pair). We account for travel time in the oceanic crust by subtracting
125 ray path distances and travel times for the portion of the path that travels through the crust,
126 assuming that all events occurred at 10 km depth (ISC catalog), and that crustal thickness is
127 uniformly 6.0 km with a crustal velocity of 6.5 km s^{-1} (Christeson *et al.*, 2019). For each station,
128 we then calculate the distance and travel time for the portion of the ray path that extends from an
129 earthquake in the crust to the Moho, and back from the Moho to the receiver. Pn velocity is
130 obtained by dividing the distance travelled in the mantle by the travel time in the mantle. Details
131 of these corrections for each station are given in Table 1.

132 Our approach yielded 152 Pn velocity estimates from the catalog of 50 regional
133 earthquakes (Figure 5). Although epicentral distances range from 32 km to \sim 1095 km, all 50 events
134 were detected at nearly all available stations, implying that the detection threshold of the combined
135 hydrophones and ASPSP station is at least M_w 3.5. Since most stations were located either near
136 to, or to the north of, the St. Paul fracture zone, our ray path coverage is more comprehensive in
137 the northern part of the study area. Ray paths sampling upper-mantle velocities to the south of the

138 St. Paul fracture zone are restricted to events detected by hydrophone EA8, and those originating
139 from four earthquakes located at the eastern end of the Romanche transform fault (Figure 5).

140

141 ***Pn* velocity uncertainty**

142 The two most significant potential sources of error in our analysis are hypocenter locations
143 of events in the ISC Catalog, and *Pn* arrival time picks. We estimated hypocenter location (and
144 hence epicentral distance) error to be ± 10 km, based upon ISC catalog location and typical error
145 in global earthquake location (Lohman and Simons, 2005; Weston *et al.*, 2012). This hypocenter
146 location error implicitly includes other uncertainties associated with ISC catalog locations, such
147 as those caused by un-modeled three-dimensional velocity structure and picking errors, which
148 result in trade-offs between origin time and location (Bondár and Storchak, 2011). Arrival time
149 pick (and hence also travel time) errors were investigated by estimating SNR for each arrival via
150 two methods, one using the amplitude ratio between peak signal and root mean square noise, and
151 another via the ratio between the short time average amplitude and long time average amplitude
152 (STA/LTA; Figure S7). We find that both SNR estimates are only weakly dependent on epicentral
153 distance and magnitude, however we do observe station-dependent variations in the scatter in SNR.
154 We quantify this scatter in terms of the standard deviation of SNR of arrivals for a particular station
155 (Figure S7e), which likely is due to persistent local noise sources. Hence we estimated arrival
156 time pick error based on the emergent character of arrivals and the standard deviation of SNR,
157 with station-dependent errors defined as ± 0.5 s for EA2 and EA8; ± 1.0 s for H2, H4 and H5; and
158 ± 0.3 s for ASPSP.

159 The total uncertainty in our velocity estimate, δv , was estimated by assuming that
160 epicentral distance, d , and travel time, t , have errors that are uncorrelated and random. This

161 assumption is valid since we attribute the main source of travel time error to uncertainty in picking
 162 of Pn arrivals (which in turn depends on waveform character and noise level), and the distance
 163 error is most significantly affected by error in earthquake location from the ISC catalog, which is
 164 assumed to be constant and hence is independent from hydrophone Pn pick error. We formally
 165 propagate the errors in d and t , as follows

$$166 \quad \delta v = v \sqrt{\left(\frac{\delta d}{d}\right)^2 + \left(\frac{\delta t}{t}\right)^2},$$

167 where δd is epicentral distance error, and δt is travel time error (e.g. Taylor, 1997).

168 Although receiver location uncertainty is negligible for the land station ASPSP (located with
 169 meter-scale accuracy via the Global Positioning System), there is potential location uncertainty for
 170 the moored hydrophones in our network. Moored hydrophone locations were obtained by acoustic
 171 triangulation between the mooring acoustic release and the deployment vessel soon after the
 172 moorings settled on the seafloor, within error of several meters. In order to account for the
 173 possibility of abnormally strong current motion, each instrument was fitted with a pressure and
 174 temperature logger below the floatation package, so that any significant hydrophone depth changes
 175 would be recorded (e.g. Fox *et al.*, 2001). Significant depth changes were not detected during
 176 deployments, and thus we assume that the hydrophone location was constant during data collection,
 177 and hence hydrophone location uncertainty is less than 10 m.

178

179 **Results**

180 ***Pn* velocities**

181 The resulting 152 Pn ray paths (Figure 5b) and travel times (Figure 6) indicates upper-
 182 mantle velocities that vary considerably across the study area, with estimates ranging between 7.2

183 and 11.1 km s^{-1} , and uncertainties ranging from 0.1 to 1.9 km s^{-1} (Table S2). Variability in reduced
184 travel time increases with epicentral distance (Figure 6), although SNR does not show a similar
185 trend (Figure S7). Hence the epicentral distance-dependent scatter in reduced travel time is likely
186 due to variations in the depth of ray penetration (which increases with epicentral distance), and not
187 due to increasing pick uncertainty. At the center of the study area there appears to be a longitudinal
188 variation in Pn velocity, with events originating near the St. Paul transform system, and sampling
189 adjacent lithosphere, having higher velocities than those from the adjacent spreading centers
190 (Figure 5a). The best constrained estimate for sub-axis, ridge-parallel mantle velocity comes from
191 ray paths that sample the portion of the spreading axis between the Strakhov fracture zone and
192 stations near the St. Paul fracture zone (H2, H5 and ASPSP). Here, Pn travel times consistently
193 imply relatively low velocities, with a mean of 7.7 km s^{-1} . Slightly higher velocities ranging
194 between 7.8 and 8.2 km s^{-1} are indicated by ray paths between hydrophone EA2 and the Strakhov
195 fracture zone, oriented roughly parallel to a plate spreading flowline. Ray paths oriented
196 southwest-northeast (azimuth $\sim 060^\circ$), i.e. oblique to the spreading direction, between events on
197 the St. Paul fracture zone and detected at hydrophone EA2, have some of the highest mantle
198 velocities (between 7.6 and 8.5 km s^{-1}) compared to other rays sampling areas unaffected by
199 fracture zones. Velocity estimates in the vicinity of the St. Paul fracture zone itself (from transform
200 faulting events detected by hydrophones H2, H4 and H5, and ASPSP) show considerable variation,
201 ranging from 8.0 to 9.1 km s^{-1} and a mean of 8.4 km s^{-1} , and little apparent spatial consistency.
202 Among these events, we encountered one of the highest Pn velocities ($9.0 \text{ km s}^{-1} \pm 0.2 \text{ s}^{-1}$) in this
203 study, for a ray path oriented roughly parallel to the St. Paul transform fault (ray azimuth $\sim 105^\circ$)
204 between an event near the St. Paul islets and detected by hydrophone H4.

205 South of the St. Paul fracture zone, ray paths from events detected by hydrophone EA8
206 showed considerable variation in upper-mantle velocity, which range from 7.2 to 9.0 km s⁻¹. Ray
207 paths originating from the spreading axis north of the St. Paul transform fault and trending ~170°
208 towards EA8, have velocities of 7.3–8.1 km s⁻¹, while ray paths from the St. Paul transform fault
209 trending ~185° towards EA8 have consistently higher velocities of 7.6–9.1 km s⁻¹.

210 Only 12 ray paths sampling the upper-mantle parallel and adjacent to the spreading axis
211 between the southern extent of the St. Paul transform fault and the Romanche transform fault are
212 available. This relatively poor coverage in ray paths in this area hinders our interpretation, where
213 velocities range from 7.2 to 8.3 km s⁻¹.

214

215 **Discussion**

216 *Upper-mantle velocity structure*

217 In general, rays originating from the St. Paul transform system have higher velocities than
218 those originating from active spreading centers to the east and west (Figure 5a), probably due to
219 cooler conditions at the Moho along the transform. Our estimates of upper-mantle *Pn* velocities
220 broadly agree (within error) with *Pn* velocities from radially stratified velocity models such as
221 PREM (Dziewonski and Anderson, 1981) and iasp91 (Figure 6; Kennett and Engdahl, 1991). Our
222 *Pn* velocity estimates are also consistent with mantle velocity estimates from a series of reversed
223 wide-angle refraction seismic profiles (i.e. with multiple shot points giving overlapping coverage)
224 collected in the equatorial Atlantic during R/V *Atlantis* cruise A180 (Figure 5b; Le Pichon *et al.*,
225 1965). The modal difference in velocity between refraction profiles from Le Pichon *et al.* (1965)
226 and all intersecting ray paths is 0.2 km s⁻¹ (see histogram in Figure 5c), although our *Pn* velocity
227 estimates are consistently lower than those reported by Le Pichon *et al.* (1965), with a maximum

228 disagreement of 1.2 km s^{-1} . A mantle velocity of 8.30 km s^{-1} was reported along profile A180-48,
229 which is 283 km-long, and crosses the eastern side of the St. Paul transform fault (near $\sim 26.3^\circ\text{W}$),
230 trending northeast-southwest (Figure 5b). This velocity is consistent with that inferred from Pn
231 ray paths with a similar orientation, originating from earthquakes on the St. Paul transform fault
232 that were detected by hydrophone EA8. Ray paths that intersect profile A180-48 (at angles either
233 perpendicular or oblique to the trend of the refraction profile) typically indicate lower upper-
234 mantle velocities, ranging from 7.3 to 8.1 km s^{-1} , with the exception of one anomalous ray path
235 oriented parallel with the St. Paul transform fault with a velocity of 9.0 km s^{-1} . Refraction profiles
236 A180-40 and -42 are oriented roughly east-west, are located ~ 100 km north of the Romanche
237 transform fault, and have velocities of 8.03 and 8.49 km s^{-1} , respectively. Although there are only
238 four Pn ray paths near to these profiles, with near-perpendicular orientation, they indicate
239 velocities ranging from 7.6 to 8.2 km s^{-1} , and hence are in broad agreement with the refraction
240 estimates. Our velocity estimates of 7.6 to 8.2 km s^{-1} are also in agreement with a velocity
241 estimate of 8.0 km s^{-1} from an active source experiment near 18°W roughly perpendicular to the
242 St. Paul fracture zone, which at this longitude separates 40 Myr old crust in the south from 70 Myr
243 old crust in the north (Growe *et al.*, 2019). The general agreement between upper-mantle velocities
244 from the refraction profiles and our Pn arrivals validates our results, and implies that spatial trends
245 observed in the study area are likely to be real.

246 Elsewhere along the MAR, between 10° to 40°N , a mean upper-mantle velocity of 8.0 km
247 $\pm 0.1 \text{ km s}^{-1}$ was estimated using a similar method to this study with Pn arrivals detected by an
248 array of autonomous hydrophones (Dziak *et al.*, 2004). Ray paths used by Dziak *et al.*, (2004)
249 often crossed the ridge axis, spanned a series of fracture zones, and extended onto older crust,

250 which may explain the close agreement in results. This result suggests that off-axis and on-axis
251 upper mantle characteristics are similar in the northern and equatorial Atlantic Ocean.

252 Near the Oceanographer transform fault on the MAR ($\sim 35^\circ\text{N}$), a two-dimensional
253 tomographic inversion of wide-angle seismic refraction data suggests velocities of $7.4\text{--}7.8\text{ km s}^{-1}$
254 (Canales *et al.*, 2000; Hooft *et al.*, 2000). These results agree within error with our estimates of Pn
255 velocity from rays sampling on-axis upper-mantle to the north of the St. Paul transform fault
256 (Figure 5b), which are typically $7.2\text{--}8.0\text{ km s}^{-1}$.

257

258 ***Upper-mantle velocity and plate age***

259 Seismic velocities in the upper-mantle near to the ridge axis, i.e. in young lithosphere, are
260 expected to be lower than in off-axis areas, due to upwelling of hot material (e.g. Turcotte and
261 Schubert, 2002). Following the removal of minor gridding artifacts associated with fracture zone
262 traces, we used a global crustal age model (Müller *et al.*, 2008) to assign a mean crustal age along
263 each ray path, for comparison with Pn velocity (Figure 7a).

264 Ray paths sampling lithosphere younger than 10 Myr show a wide range of velocities, with
265 a mean of 7.9 km s^{-1} and standard deviation of 0.5 km s^{-1} . Twenty ray paths yield velocities less
266 than 7.5 km s^{-1} . Pn velocities for ray paths sampling lithosphere older than 20 Myr are slightly
267 higher, with a mean of 8.1 km s^{-1} and standard deviation of 0.3 km s^{-1} , while only two ray paths
268 give velocities lower than 7.5 km s^{-1} (Figure 7a). Most rays cover a wide range of crustal ages, so
269 this geometry, and our averaging approach, may smear the possible effects of lithospheric aging.
270 The lack of rays travelling exclusively via older lithosphere may also obscure any progressive
271 trend between upper-mantle velocity and crustal age. However, the tendency toward the inclusion

272 of lower velocities in younger crust (Figure 7a) reflects the expected variation with respect to the
273 zone of axial upwelling.

274

275 ***Azimuthal Seismic Anisotropy***

276 Laboratory experiments have shown that the mantle can experience significant shear strain
277 during corner flow at the ridge axis, leaving an anisotropic fabric in the lithospheric mantle as
278 minerals (e.g. olivine) are aligned into a lattice preferred orientation (LPO; e.g. Zhang and Karato,
279 1995; Nicolas and Christensen, 2011). Anisotropy consistent with a LPO formed by two-
280 dimensional mantle flow has been measured at some locations in the oceanic upper mantle, in
281 particular at the fast-spreading East Pacific Rise (e.g. Raitt *et al.*, 1969; Lin *et al.*, 2016), however
282 the strength of anisotropy varies widely, and debate remains about its origins (e.g. Mark *et al.*,
283 2019). Since isochrons in this region are fairly uniform (Figure 5), V_{Pn} anisotropy could be
284 expected parallel to paleo-relative plate motion, although this assumption has been shown to not
285 apply everywhere (VanderBeek and Toomey, 2017).

286 We investigated the dependence of mantle velocity with azimuth, and use epicentral
287 distance as a proxy for depth of mantle penetration to group rays (Figure 7b). No discernable
288 pattern is evident in rays grouped by epicentral distance, including those expected to sample
289 deepest in the mantle with epicentral distances > 700 km (blue lines in Figure 7c). Removing rays
290 with V_{Pn} error > 0.4 km s $^{-1}$ also does not resolve any azimuthal dependence (Figure 7d), nor does
291 separating rays by mean crustal age (Figures 7e and 7f).

292 The apparent lack of such azimuthal dependence could be due to several reasons. First,
293 azimuthal dependence may be too subtle to be resolved by our V_{Pn} estimates, given the
294 uncertainties in hypocenter location and crustal thickness discussed above. Second, the slow

295 spreading rate of the MAR (~ 32 mm yr $^{-1}$ total rate; (DeMets *et al.*, 2010)) may result in a thickened
296 lithosphere that is dominantly cooled by conduction, thus inhibiting corner flow (e.g. Sleep, 1975).
297 As a result, deformation could be accommodated by faulting at depths of 5–10 km beneath the
298 Moho, reducing the viscous strain in the mantle at these depths, and suppressing the anisotropy
299 recorded in the mantle (e.g. Ribe, 1989). Observations of weaker or anomalous anisotropy
300 elsewhere in the Atlantic Ocean are consistent with our findings (e.g. Gaherty *et al.*, 2004; Dunn
301 *et al.*, 2005). Third, complex, three-dimensional upwelling patterns near the ridge axis could result
302 in anisotropy on relatively short wavelengths (Lin and Phipps Morgan, 1992), which would be
303 smeared along our relatively long ray paths, and hence not be resolved.

304

305 ***Pn and surface wave velocity***

306 To explore the relationship between V_{Pn} and the thermal structure of the asthenospheric
307 upper-mantle, we compared our velocity estimates with a global, vertically polarized shear speed
308 model SL2013sv (Schaeffer and Lebedev, 2013). Our objective is to evaluate our observations of
309 uppermost mantle properties in the context of deeper mantle properties. We do not aim to directly
310 validate our V_{Pn} estimates via this comparison. This model was chosen because it is particularly
311 sensitive to anomalies within the upper-mantle, and hence provides a window into the upper mantle
312 structure directly beneath our Pn ray paths (Schaeffer and Lebedev, 2013). We extracted values
313 of vertically polarized tomographic shear velocity anomaly (% dVs) at 100 km intervals along each
314 ray path, from slices through the SL2013sv model at depths of 25, 50, 75 and 150 km. We then
315 calculated the mean % dVs along each ray path, at each depth interval (Figure 8). At 25 and 50
316 km depths, the effects of the ridge axis are evident, with higher velocities associated with ray paths
317 travelling off-axis (detected by EA2 and EA8), and hence not sampling the relatively low-velocity

318 axial region (Figures 8a and 8b). This effect is less pronounced at 75 km depth (Figure 8c), and is
319 not apparent at 150 km depth, which presumably reflects sub-plate velocities. The lack of
320 correlation between SL2013sv and Pn velocities at 150 km suggests that our V_{Pn} estimates,
321 sensitive to the velocity structure directly beneath the Moho, do not record deeper, larger-scale
322 sub-plate (i.e. asthenospheric) processes and anomalies. Hence our observed V_{Pn} variability may
323 instead arise due to local variations in melt supply, lithospheric thickness, or faulting.

324

325 **Conclusions**

326 We used a network of five autonomous hydrophones and a broadband seismograph to detect
327 Pn arrivals from regional earthquakes in the equatorial Atlantic Ocean over a period of ~12 months
328 between 2012 and 2013. Our estimates of upper-mantle velocity from the travel times of 152 Pn
329 arrivals broadly agree (mostly within 0.2 km s^{-1}) with those from nearby seismic refraction
330 experiments.

331 We find that the upper-mantle near the St. Paul transform system has consistently high
332 velocities ($>8 \text{ km s}^{-1}$), compared to relatively low velocities ($\sim 7.5 \text{ km s}^{-1}$) in the adjacent MAR
333 spreading segments northwest of the transform. This spatial pattern is consistent with the notion
334 that Pn ray paths sample lower velocity mantle near the ridge axis, and higher velocity material
335 near transforms, which are generally cooler, despite the presence of intra-transform spreading
336 segments. We do not resolve any dependence between V_{Pn} and azimuth, which could either be
337 due to observational uncertainty, or due to the combined effects of thickened lithosphere and more
338 complex mantle upwelling patterns under slow-spreading conditions. We also do not find any
339 correlation between V_{Pn} and vertically polarized shear speed from the global SL2013sv model,
340 indicating that our method is not sensitive to properties of the asthenosphere. The close agreement

341 between our results and those from seismic refraction experiments demonstrates that the relatively
342 simple method of using sparse arrays of autonomous hydrophones to detect Pn arrivals can be used
343 to obtain accurate estimates of upper-mantle velocities. Hence, this method provides a useful
344 complement to deployments of other seafloor instruments such as ocean bottom seismographs, in
345 remote areas where direct observations are typically elusive.

346

347 **Data and Resources**

348 All Pn velocities obtained in this study using the hydrophones data of the COLMEIA/EA array
349 (Smith *et al.*, 2012; Maia *et al.*, 2014) and the seismic records of the and ASPSP station (de Melo
350 and do Nascimento., 2018), are presented in tables of Supplemental Material. Analysis and figure
351 preparation were carried out using the Generic Mapping Tools version 5.4.5 (Wessel *et al.*, 2013),
352 Seismic Analysis Code (Helffrich *et al.*, 2013). Earthquake locations used in this work were
353 obtained from the International Seismological Center Bulletin database at
354 www.isc.ac.uk/iscbulletin/search/bulletin/ (last accessed November 2019). The Global Centroid
355 Moment Tensor Project database of Ekström *et al.* (2012) was searched
356 using www.globalcmt.org/CMTsearch.html (last accessed November 2019).

357

358

359 **Acknowledgements**

360 This research was supported by National Science Foundation grants EAR-1062238, EAR-1062165
361 and OCE-1839727, and by an InterRidge Student Fellowship for GWSdM. The COLMEIA
362 expedition was funded by the French Ministry of Research through its grant to the French
363 Oceanographic Fleet. COLMEIA hydrophone deployment was funded by LABEX MER grant

364 “Actions à la mer”, and instruments were recovered with the help of the Brazilian Navy. AFdN
365 thanks the support of the Brazilian Navy and CNPq for grants 392484441/2012-4 and
366 303817/2014-3. This paper is NOAA/Pacific Marine Environmental Laboratory contribution
367 number 5116. We thank Associate Editor, T. Brocher, B. VanderBeek, and an anonymous reviewer
368 for their constructive input. Any opinion, findings, and conclusions or recommendations
369 expressed in this material are those of the authors and do not necessarily reflect the views of the
370 National Science Foundation.

371

372 **References**

- 373 Abercrombie, R. E., and G. Ekstrom (2001). Earthquake slip on oceanic transform faults, *Nature*
374 **410**, 74–77.
- 375 Barlow, J. (2019). Global Ocean Sound Speed Profile Library (GOSSPL), an Rdata resource for
376 studies of ocean sound propagation, *NOAA Tech. Memo. NMFS SWFSC* **612**, no. March, 1–
377 7, doi: 10.25923/7DJ1-J540.
- 378 Bondár, I., and D. Storchak (2011). Improved location procedures at the International
379 Seismological Centre, *Geophys. J. Int.* **186**, no. 3, 1220–1244, doi: 10.1111/j.1365-
380 246X.2011.05107.x.
- 381 Brandsdottir, B., and W. Menke (1997). Faroe-Iceland Ridge Experiment, 2, Crustal structure of
382 the Krafla central volcano, *J. Geophys. Res.* **102**, no. B4, 7867–7886.
- 383 Campos, T., F. H. R. Bezerra, N. K. Srivastava, M. M. Vieira, and C. Vita-Finzi (2010). Holocene
384 tectonic uplift of the St Peter and St Paul Rocks (Equatorial Atlantic) consistent with
385 emplacement by extrusion, *Mar. Geol.* **271**, no. 1–2, 177–186, doi:
386 10.1016/j.margeo.2010.02.013.
- 387 Canales, J. P., J. A. Collins, and R. S. Detrick (2000). Seismic structure across the rift valley of
388 the Mid-Atlantic Ridge at 23°20' (MARK area): Implications for crustal accretion processes
389 at slow spreading ridges, *J. Geophys. Res.* **105**, no. B12, 28411–28425, doi:
390 10.1029/2000JB900301.
- 391 Christeson, G. L., J. A. Goff, and R. S. Reece (2019). Synthesis of Oceanic Crustal Structure
392 From Two-Dimensional Seismic Profiles, *Rev. Geophys.* **57**, doi: 10.1029/2019RG000641.
- 393 Chulick, G. S., S. Detweiler, and W. D. Mooney (2013). Seismic structure of the crust and
394 uppermost mantle of South America and surrounding oceanic basins, *J. South Am. Earth*

- 395 *Sci.* **42**, 260–276, doi: 10.1016/j.jsames.2012.06.002.
- 396 Chulick, G. S., and W. D. Mooney (2002). Seismic Structure of the Crust and Uppermost Mantle
397 of North America and Adjacent Oceanic Basins: A Synthesis, *Bull. Seismol. Soc. Am.* **92**,
398 no. 6, 2478–2492, doi: 10.1016/j.jsames.2012.06.002.
- 399 D'Eu, J. F., J. Y. Royer, and J. Perrot (2012). Long-term autonomous hydrophones for large-scale
400 hydroacoustic monitoring of the oceans, in *Proceedings of Oceans, 2012-Yeosu*, IEEE, 1–6,
401 doi: 10.1109/OCEANS-Yeosu.2012.6263519.
- 402 DeMets, C., R. G. Gordon, and D. F. Argus (2010). Geologically current plate motions, *Geophys.*
403 *J. Int.* **181**, 1–80, doi: 10.1111/j.1365-246X.2009.04491.x.
- 404 Dunn, R. A., V. Lekić, R. S. Detrick, and D. R. Toomey (2005). Three-dimensional seismic
405 structure of the Mid-Atlantic Ridge (35°N): Evidence for focused melt supply and lower
406 crustal dike injection, *J. Geophys. Res. Solid Earth* **110**, no. 9, 1–17, doi:
407 10.1029/2004JB003473.
- 408 Dziak, R. P., D. R. Bohnenstiehl, H. Matsumoto, C. G. Fox, D. K. Smith, M. Tolstoy, T. K. Lau,
409 J. H. Haxel, and M. J. Fowler (2004). P- and T-wave detection thresholds, Pn velocity
410 estimate, and detection of lower mantle and core P-waves on ocean sound-channel
411 hydrophones at the Mid-Atlantic Ridge, *Bull. Seism. Soc. Am.* **94**, no. 2, 665–677, doi:
412 10.1785/0120030156.
- 413 Dziewonski, A. M., and D. L. Anderson (1981). Preliminary reference Earth model, *Phys. Earth*
414 *Planet. Inter.* **25**, 297–356.
- 415 Ekström, G., M. Nettles, and A. M. Dziewoński (2012). The global CMT project 2004–2010:
416 Centroid-moment tensors for 13,017 earthquakes, *Phys. Earth Planet. Inter.* **200–201**, 1–9,
417 doi: 10.1016/j.pepi.2012.04.002.

- 418 Fox, C. G., H. Matsumoto, and T.-K. A. Lau (2001). Monitoring Pacific Ocean seismicity from
419 an autonomous hydrophone array, *J. Geophys. Res.* **106**, no. 10, 41834206, doi:
420 10.1029/2000JB900404.
- 421 Francis, T. J. G., I. T. Porter, and R. C. Lilwall (1978). Microearthquakes near the eastern end of
422 St Paul's fracture zone, *Geophys. J. R. Astron. Soc.* **53**Reprint, 201–217.
- 423 Gaherty, J. B., D. Lizarralde, J. A. Collins, G. Hirth, and S. Kim (2004). Mantle deformation
424 during slow seafloor spreading constrained by observations of seismic anisotropy in the
425 western Atlantic, *Earth Planet. Sci. Lett.* **228**, no. 3–4, 255–265, doi:
426 10.1016/j.epsl.2004.10.026.
- 427 Gasperini, L., G. Carrara Marco Ligi, P. Fabretti, D. Brunelli, A. Cipriani, S. Susini, and P.
428 Tartarotti (1997). New data on the geology of the Romanche FZ., equatorial Atlantic:
429 PRIMAR-96 cruise report, **3**, no. 59, 1–2.
- 430 Growe, K., I. Grevemeyer, S. Singh, and C. Papenberg (2019). Seismic structure of the St . Paul
431 Fracture Zone near 18°W in the Atlantic Ocean – evidence for a magmatic origin of crust,
432 *Geophys. Res. Abstr.* **21**, 4770.
- 433 Helffrich, G., J. Wookey, and I. Bastow (2013). *The Seismic Analysis Code: A Primer and User's*
434 *Guide*, Cambridge, UK.
- 435 Hooft, E. E. E., R. S. Detrick, D. R. Toomey, J. A. Collins, and J. Lin (2000). Crustal thickness
436 and structure along three contrasting spreading segments of the Mid-Atlantic Ridge, 33.5°–
437 35°N, *J. Geophys. Res. Solid Earth* **105**, no. B4, 8205–8226, doi: 10.1029/1999jb900442.
- 438 Kennett, B. L. N., and E. R. Engdahl (1991). traveltimes for global earthquake location and
439 phase identification, *Geophys. J. Int.* **105**, no. 2, 429–465, doi: 10.1111/j.1365-
440 246X.1991.tb06724.x.

- 441 Lin, P. Y. P., J. B. Gaherty, G. Jin, J. A. Collins, D. Lizarralde, R. L. Evans, and G. Hirth (2016).
- 442 High-resolution seismic constraints on flow dynamics in the oceanic asthenosphere, *Nature*
443 **535**, no. 7613, 538–541, doi: 10.1038/nature18012.
- 444 Lin, J., and J. Phipps Morgan (1992). The spreading rate dependence of three-dimensional mid-
445 ocean ridge gravity structure, *Geophys. Res. Lett.* **19**, no. 1, 13–16.
- 446 Linehan, D. (1940). Earthquakes in the West Indian region, *Eos Trans. AGU* **21**, no. 2, 229–232,
447 doi: doi:10.1029/TR021i002p00229.
- 448 Lohman, R. B., and M. Simons (2005). Locations of selected small earthquakes in the Zagros
449 mountains, *Geochemistry, Geophys. Geosystems* **6**, no. 3, doi: 10.1029/2004GC000849.
- 450 Maia, M., I. Brehme, U. F. Fluminense, A. Briais, and D. Brunelli (2014). Preliminary report on
451 the COLMEIA Cruise, Equatorial Atlantic Recife, January 24 - Recife, February 28, 2013,
452 *InterRidge News* **22**, 52–56, doi: 10.1029/2005JB004210.Von.
- 453 Maia, M., S. Sichel, A. Briais, D. Brunelli, M. Ligi, N. Ferreira, T. Campos, B. Mougel, I.
454 Brehme, C. Hémond, *et al.* (2016). Extreme mantle uplift and exhumation along a
455 transpressive transform fault, *Nat. Geosci.* **9**, no. 8, 619–623, doi: 10.1038/ngeo2759.
- 456 Mark, H. F., D. Lizarralde, J. A. Collins, N. C. Miller, G. Hirth, J. B. Gaherty, and R. L. Evans
457 (2019). Azimuthal Seismic Anisotropy of 70-Ma Pacific-Plate Upper Mantle, *J. Geophys.*
458 *Res. Solid Earth* **124**, no. 2, 1889–1909, doi: 10.1029/2018JB016451.
- 459 de Melo, G., and A. F. do Nascimento (2018). Earthquake Magnitude Relationships for the Saint
460 Peter and Saint Paul Archipelago, Equatorial Atlantic, *Pure Appl. Geophys.* **175**, no. 3, 741–
461 756, doi: 10.1007/s00024-017-1732-6.
- 462 Müller, R. D., M. Sdrolias, C. Gaina, and W. R. Roest (2008). Age, spreading rates, and
463 spreading asymmetry of the world's ocean crust, *Geochem. Geophys. Geosyst* **9**, no. 4, 1–

- 464 19, doi: 10.1029/2007GC001743.
- 465 Nicolas, A., and N. I. Christensen (2011). Formation of anisotropy in upper mantle peridotites - A
466 review, in *Composition, structure and dynamics of the lithosphere-asthenosphere system, Geodynamics* K. Fuchs, and C. Froidevaux(Editors), American Geophysical Union,
467 Washington, D. C., 111–123, doi: 10.1029/gd016p0111.
- 468
- 469 Le Pichon, X., R. E. Houtz, C. L. Drake, and J. E. Nafe (1965). Crustal structure of the mid-
470 ocean ridges: 1. Seismic refraction measurements, *J. Geophys. Res.* **70**, no. 2, 319–339, doi:
471 10.1029/jz070i002p00319.
- 472 Raitt, R. W., J. Shor, G. G., T. J. G. Francis, and G. B. Morris (1969). Anisotropy of the Pacific
473 upper mantle, *J. Geophys. Res.* **74**, no. 12, 3095–3109, doi:
474 <https://doi.org/10.1029/JB074i012p03095>.
- 475 Ribe, N. M. (1989). Seismic anisotropy and mantle flow, *J. Geophys. Res.* **94**, no. B4, 4213–
476 4223, doi: 10.1029/JB094iB04p04213.
- 477 Schaeffer, A. J., and S. Lebedev (2013). Global shear speed structure of the upper mantle and
478 transition zone, *Geophys. J. Int.* **194**, no. 1, 417–449, doi: 10.1093/gji/ggt095.
- 479 Sleep, N. H. (1975). Formation of Oceanic Crust: Some Thermal Constraints, *J. Geophys. Res.*
480 **80**, no. 29, 4037–4042.
- 481 Smith, D. K., R. P. Dziak, C. Palmiotto, R. Parnell-Turner, and A. Zhelezov (2012). The
482 seismicity of the equatorial Mid-Atlantic Ridge and its long-offset transforms, *Abstr: OS13B-1720 Present. 2012 Fall Meet. AGU, San Fr. Calif. 5-9 Dec.*
- 483
- 484 Taylor, J. (1997). *Introduction to Error Analysis, the Study of Uncertainties in Physical*
485 *Measurements*, University Science Books, New York, NY.
- 486 Turcotte, D. L., and G. Schubert (2002). *Geodynamics*, Cambridge University Press, doi:

- 487 10.1017/CBO9780511807442.
- 488 Udintsev, G. B., H. J., V. G. Udintsev, and A. B. Knjazev (1996). Topography of the Equatorial
489 Segment of the Mid-Atlantic Ridge After Multi-Beam Echo-sounding., in *Equatorial*
490 *Segment of the Mid-Atlantic Ridge: IOC Technical Series No. 46* G. B. Udintsev(Editor),
491 United Nations Educational, Scientific and Cultural Organization, Paris, France, 8–15.
- 492 VanderBeek, B. P., and D. R. Toomey (2017). Shallow Mantle Anisotropy Beneath the Juan de
493 Fuca Plate, *Geophys. Res. Lett.* **44**, no. 22, 11,382–11,389, doi: 10.1002/2017GL074769.
- 494 Wessel, P., W. H. F. Smith, R. Scharroo, J. Luis, and F. Wobbe (2013). Generic Mapping Tools:
495 Improved Version Released, *Eos Trans. AGU* **94**, no. 45, 409–410.
- 496 Weston, J., A. M. G. Ferreira, and G. J. Funning (2012). Systematic comparisons of earthquake
497 source models determined using InSAR and seismic data, *Tectonophysics* **532–535**, 61–81,
498 doi: 10.1016/j.tecto.2012.02.001.
- 499 Zhang, Z., and S. Karato (1995). Lattice preferred orientation of olivine aggregates in simple
500 shear, *Nature* **375**, 774–777.
- 501

502 **Author mailing addresses**

503

504 Departamento de Geofisica, Federal University of Rio Grande do Norte, Natal, Brazil

505 (GWSdM, AFN)

506 Institute of Geophysics and Planetary Physics, Scripps Institution of Oceanography, University of

507 California, San Diego, CA, USA

508 (RPT)

509 NOAA, Pacific Marine Environmental Laboratory, Newport, OR, USA

510 (RPD)

511

512 National Science Foundation, Alexandria, VA, USA

513 (DKS)

514

515 Laboratoire Geosciences Ocean, CNRS and University of Brest

516 LGO-IUEM, rue Dumont Durville, 29280 Plouzane, France

517 (MM and JYR)

518

519

520

521 **Table 1.** Details of seismograph (S) and hydrophone (H) sensors used for Pn analysis. Sensor
 522 depth is given below sea level (bsl); water delay is based upon cable length, and water/crust
 523 corrections are applied to each Pn ray path individually.

524

Station name	Sensor type	Lat, °N	Lon, °E	Depth bsl, m	Cable length, m	Water delay, s	Crust path correction, km	Crust travel time correction, s
ASPSP	S	0.9169	-29.3459	-16	-	-	12.5	1.9
EA2	H	4.9907	-22.9931	800	3912	2.10	23.8	7.2
EA8	H	-2.5159	-29.2181	800	3242	2.54	23.0	6.5
H2	H	1.3297	-31.3445	700	2260	1.57	21.8	5.5
H4	H	0.4123	-24.6437	700	1860	1.24	21.3	5
H5	H	0.1552	-27.7875	700	3060	2.04	22.8	6.3

525

526

527

528

529

530

531

532

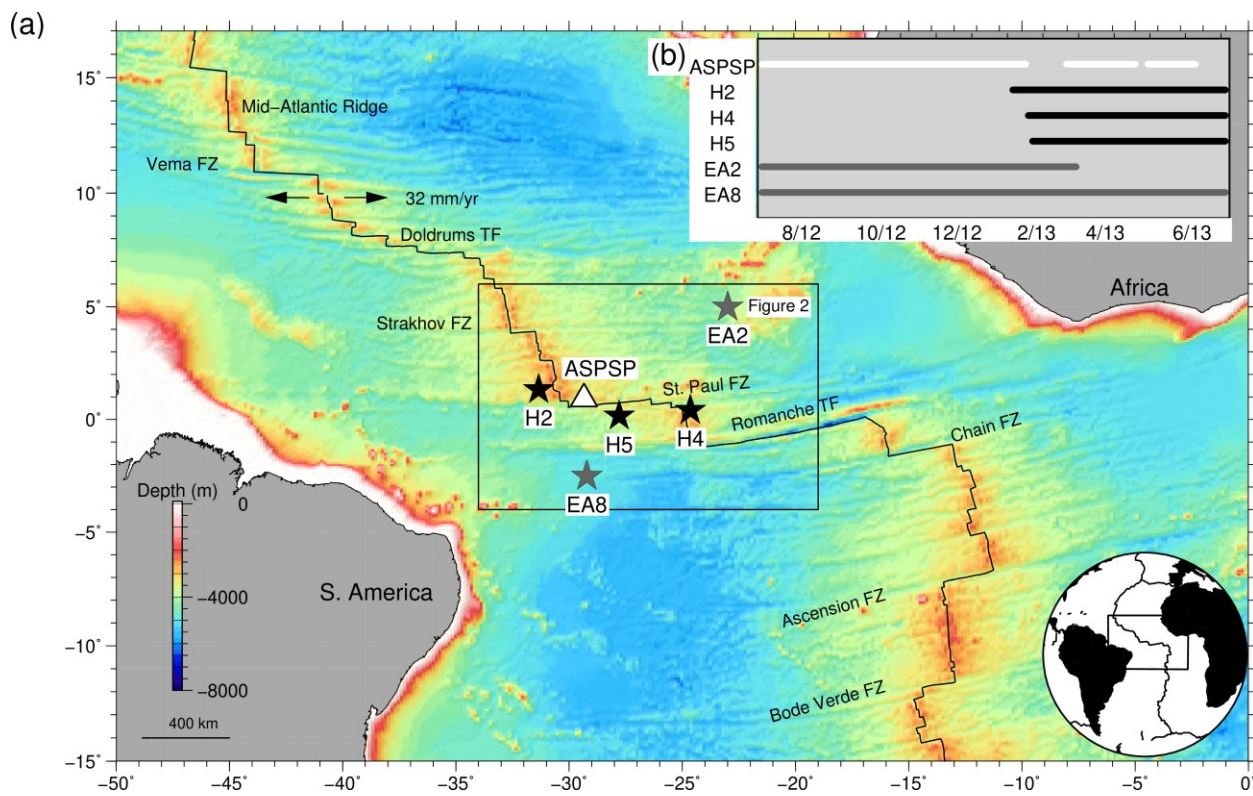
533

534

535

536

537

538 **Figures**

539

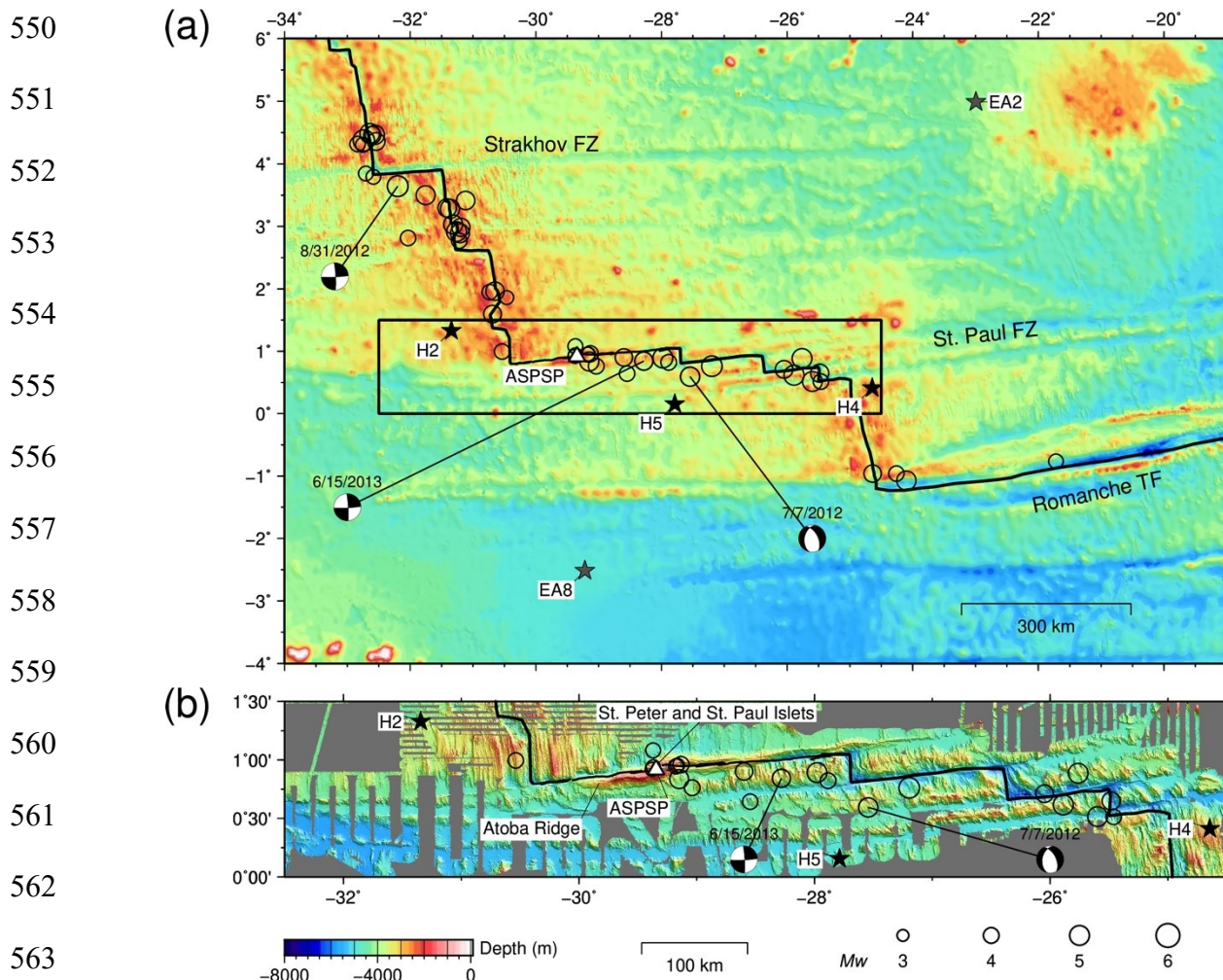
540

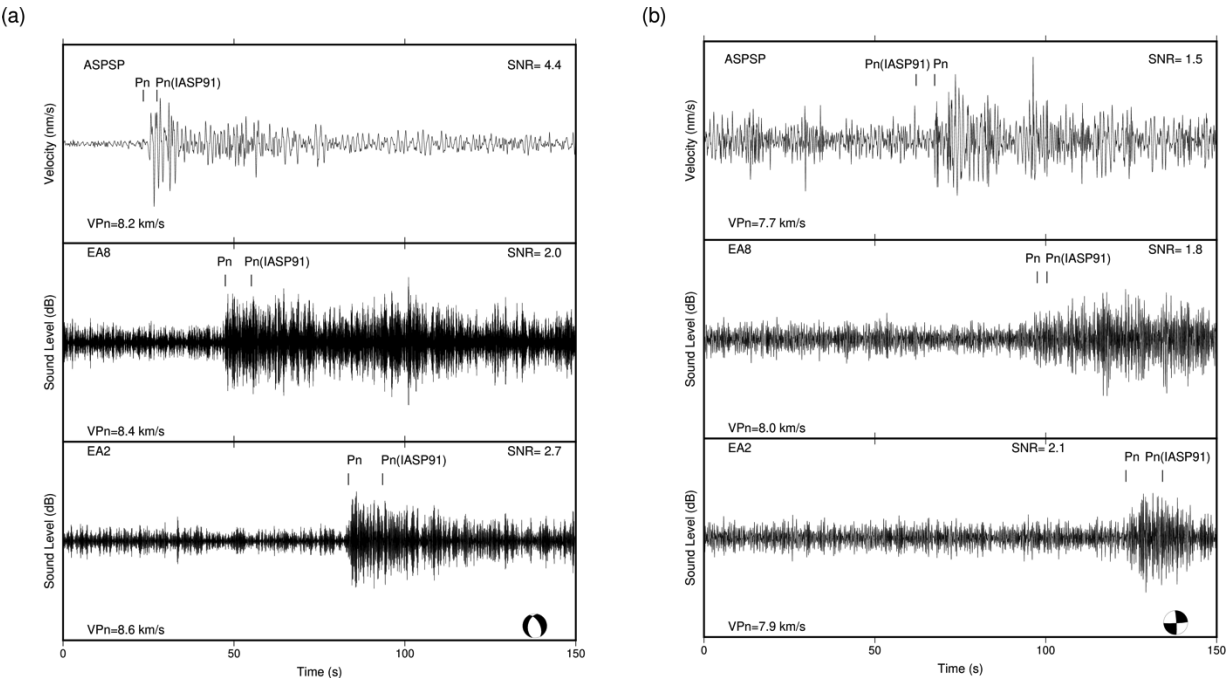
541 **Figure 1. a)** Regional bathymetric map of equatorial Atlantic ocean. White triangle shows
 542 ASPSP seismograph station, located on St. Peter and St. Paul islets; black/gray stars are
 543 COLMEIA / EA hydrophone networks, respectively (Smith *et al.*, 2012; Maia *et al.*, 2014); black
 544 line is Mid-Atlantic Ridge, with selected transforms and half-spreading rate noted (arrows).
 545 Black box shows location of Figure 2. **b)** Bars show instrument recording intervals: ASPSP
 546 (white), COLMEIA (black), and EA (gray).

547

548

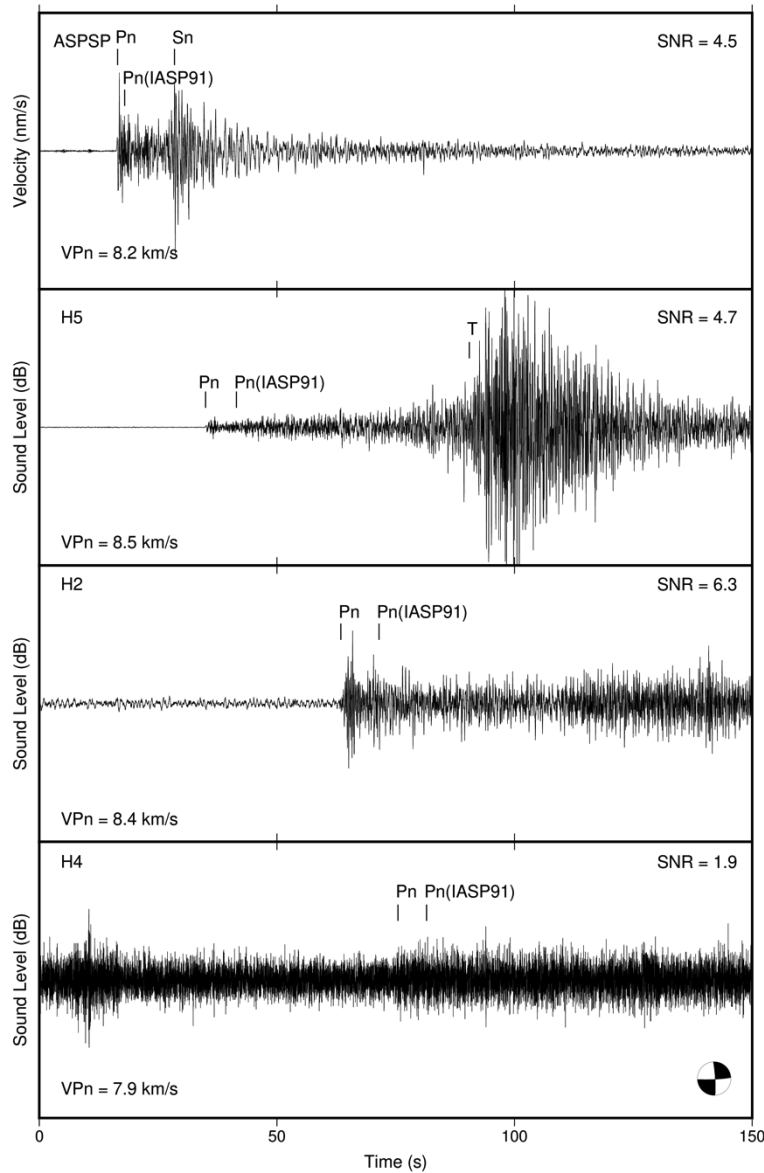
549





573

574 **Figure 3.** Example waveforms recorded by the ASPSP seismograph and EA array hydrophones,
 575 with 4–12 Hz and 6–20 Hz Butterworth filters applied, respectively. **a)** M_w 4.9 normal faulting
 576 event on 7th July 2012, located on the St. Paul transform fault at 27.5°W. Picked *Pn* arrivals, and
 577 *Pn* arrivals predicted by iasp91 model are marked; beach-balls are centroid moment tensors
 578 (Ekström et al., 2012); V_{Pn} and signal to noise ratio (SNR) noted for each station (this study),
 579 SNR calculated STA/LTA. **b)** Mw 5.3 strike-slip event on 31st August 2012, located on Strakhov
 580 transform fault near 32.5°W.

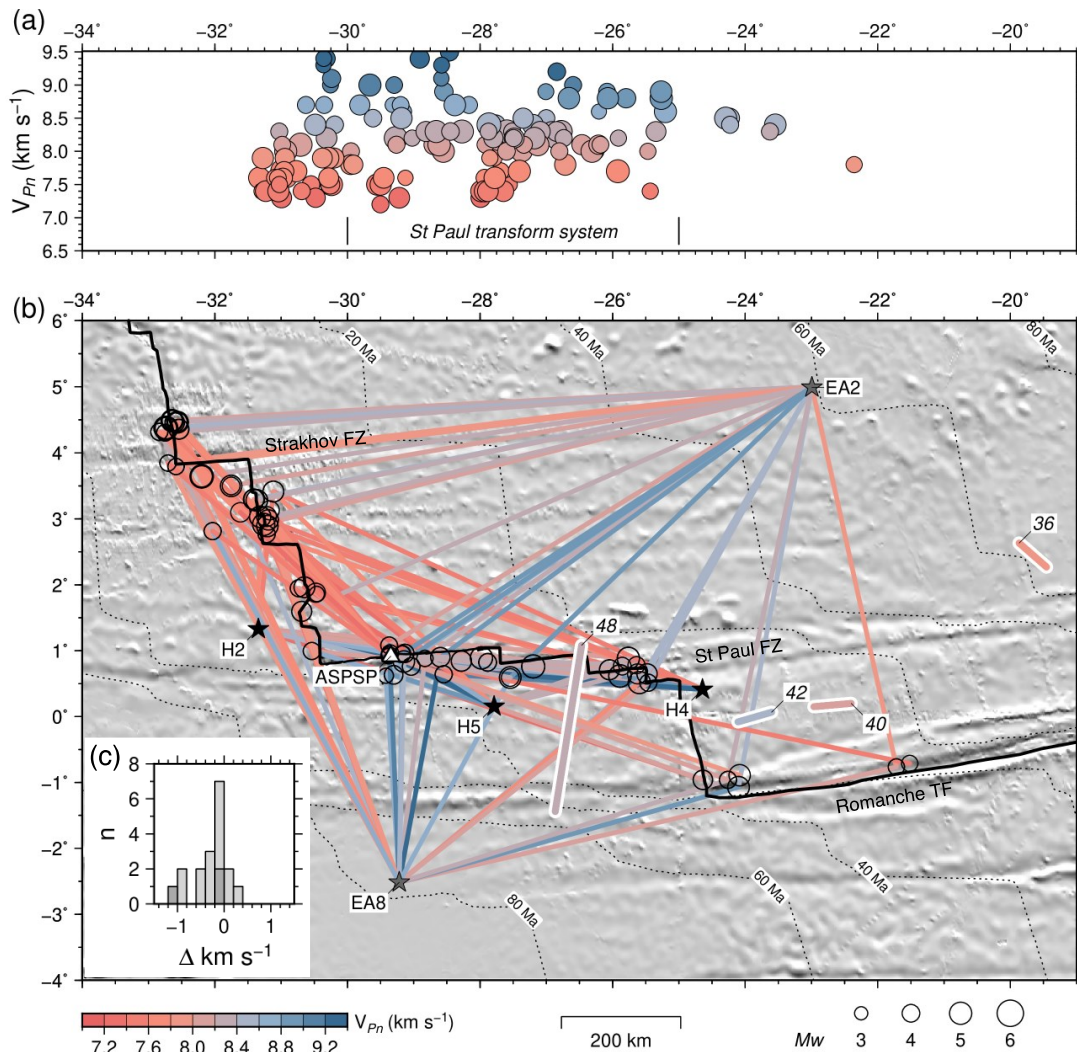


581

582

583 **Figure 4.** Example of waveforms recorded by the ASPSP seismograph and COLMEIA
 584 hydrophones, with 4–12 Hz and 6–20 Hz Butterworth filters applied, respectively, for mb 4.6
 585 strike-slip event on 15th June 2013, located near St. Paul transform fault at 29.5°W. Picked P_n
 586 arrivals, and P_n arrivals predicted by iasp91 model are marked; beach-balls are centroid moment
 587 tensors (Ekström et al., 2012); V_{P_n} and SNR noted for each station (this study).

588

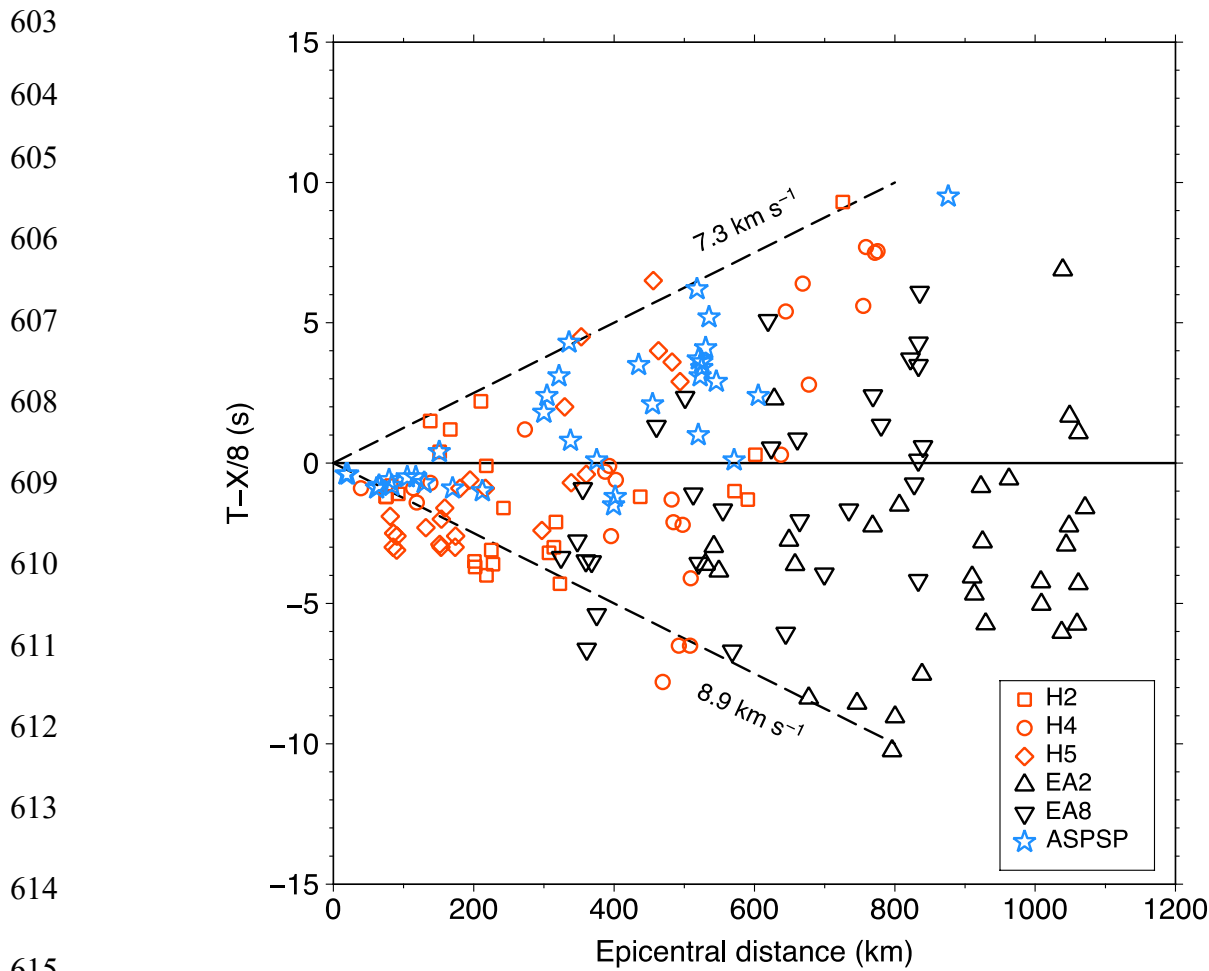


589

590

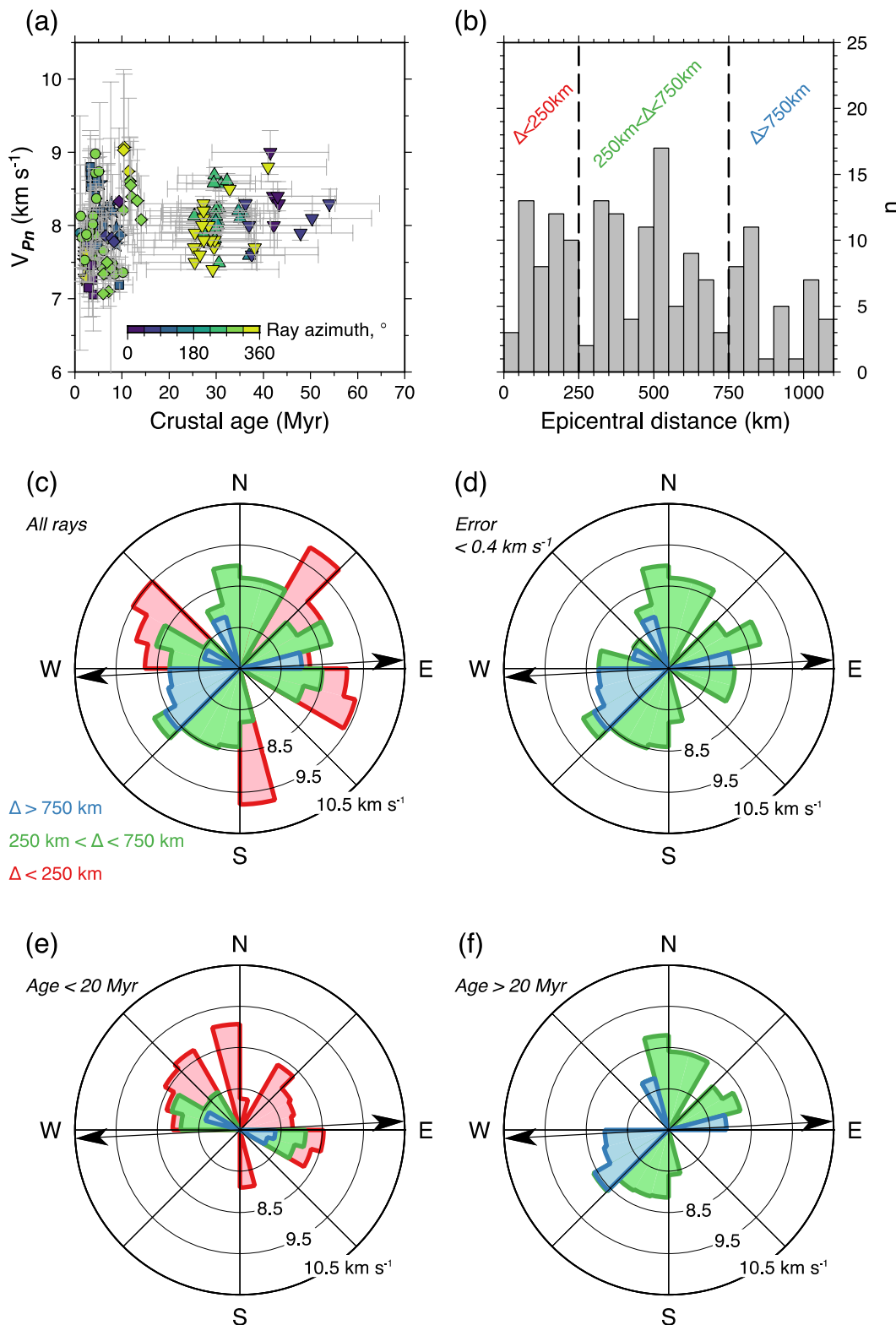
591 **Figure 5. a)** V_{Pn} plotted against mean longitude of ray path. Circle radius scaled by magnitude
 592 of source event; colored by V_{Pn} ; St. Paul transform system marked by vertical bars. **b)** Shaded
 593 relief map showing stations, earthquakes, and ray paths. Circles are earthquakes used in Pn
 594 analysis, scaled by M_w ; colored lines are ray paths shaded by Pn velocity; white triangle is
 595 ASPSP station; black/gray stars are COLMEIA / EA hydrophone networks, respectively; thick
 596 lines numbered 48, 42, 40, and 36 are seismic refraction profiles from cruise AT40-180 (Le
 597 Pichon *et al.*, 1965), shaded by velocity; dotted lines are isochrons, modified from Müller *et al.*
 598 (2008) to remove artifacts associated with fracture zone traces. **c)** Histogram of difference

599 between velocity estimates from refraction experiment (Le Pichon *et al.*, 1965), and intersecting
600 ray paths from this study; positive values indicate higher velocities estimated by refraction
601 experiment; dark/light gray bars are velocities from profiles AT40-180 48 and 42, respectively.
602



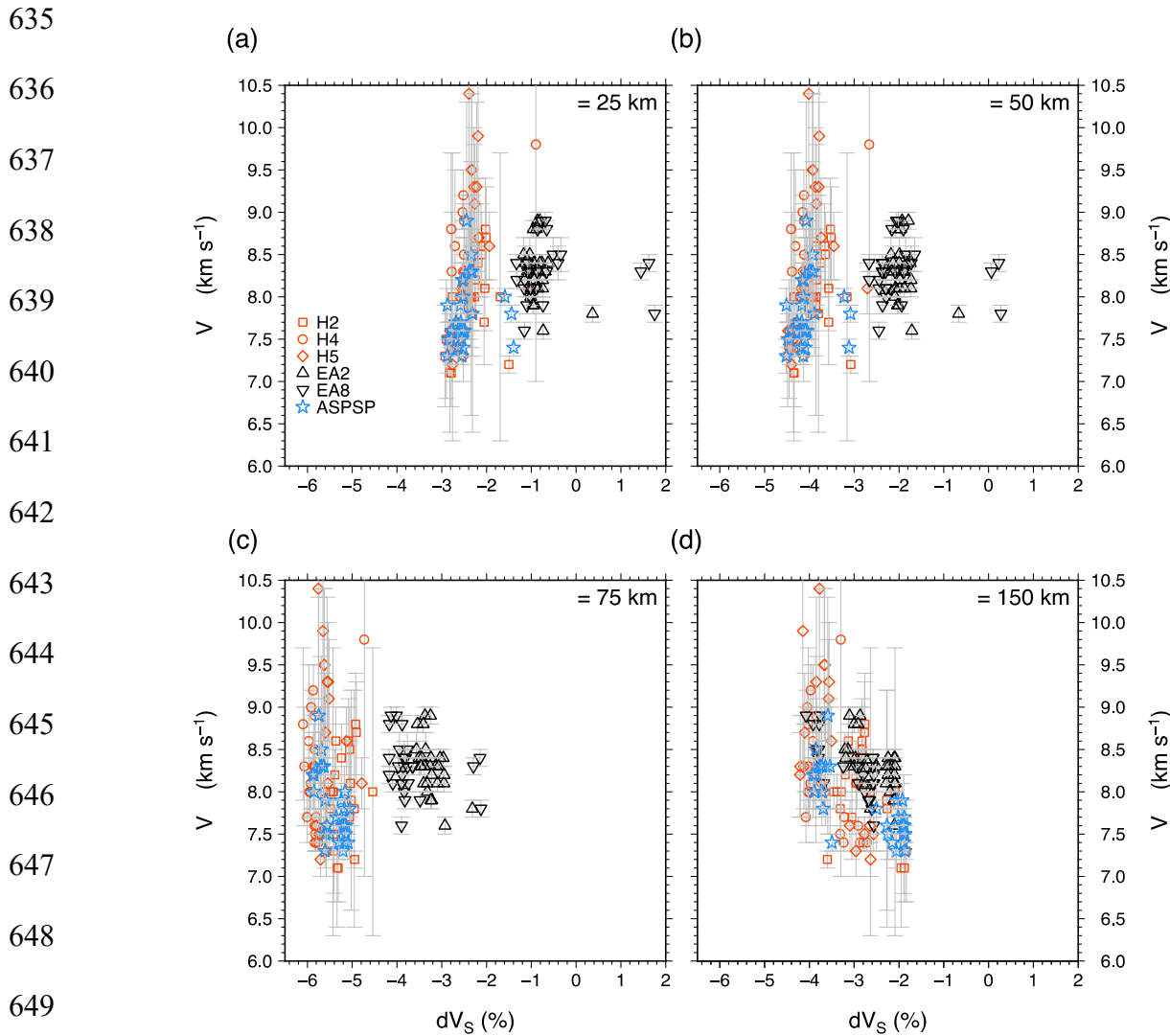
617 **Figure 6.** Reduced travel time versus epicentral distance, plotted with a reduction velocity of 8
 618 km s^{-1} , approximately corresponding to velocity immediately below Moho from PREM and
 619 iasp91 models (solid line; Dziewonski and Anderson, 1981; Kennett and Engdahl, 1991); dashed
 620 lines show velocity bounds of 7.3 and 8.9 km s^{-1} ; key shows recording station symbols.

621



624 **Figure 7. a)** V_{Pn} plotted against oceanic crustal age at epicentral location, colored by ray azimuth
625 (crustal ages assigned from model of Müller *et al.*, 2008); key for station symbols given in Figure
626 6; horizontal error bars are 2σ crustal age along ray path, vertical error bars are V_{Pn} uncertainty
627 described in text. **b)** Histogram of epicentral distances; dotted lines show cut-offs used to define
628 categories in anisotropy analysis. **c)** Sector diagram showing V_{Pn} vs. azimuth for all rays; length
629 of sectors scaled by median V_{Pn} , calculated in 15° bins, and colored by epicentral distance category;
630 black arrows show plate spreading vector. **d)** Median V_{Pn} vs. azimuth for rays with V_{Pn} uncertainty
631 $< 0.4 \text{ km s}^{-1}$, colored by epicentral distance category. **e)** Median V_{Pn} vs. azimuth for rays sampling
632 crust $< 20 \text{ Myr}$ in age, colored by epicentral distance category. **f)** Median V_{Pn} vs. azimuth for rays
633 sampling crust $> 20 \text{ Myr}$ in age, colored by epicentral distance category.

634



651 **Figure 8 (a-d)** Relationship between V_{Pn} and vertically polarized tomographic shear velocity
 652 anomaly at depths of 25, 50, 75 and 150 km, respectively, from global model SL2013sv (Schaeffer
 653 and Lebedev, 2013).